Computers and Structures 256 (2021) 106641

Contents lists available at ScienceDirect

Computers and Structures

journal homepage: www.elsevier.com/locate/compstruc

Stress and stiffness-based topology optimization of two-material thermal structures

Ali Y. Tamijani

Embry-Riddle Aeronautical University, Daytona Beach, FL 32114, United States

ARTICLE INFO

Article history:
Received 9 June 2020
Accepted 12 July 2021

Keywords:
Topology optimization
Multi-material
Stress constraint
Thermal load
Additive manufacturing

ABSTRACT

Gradient additive manufacturing techniques are capable of implementing multiple materials with graded compositions into the fabrication of a single component. This provides a unique opportunity to control the properties of materials, such as thermal expansion, Young's modulus, and yield stress, and create a structure that otherwise would be infeasible. To utilize this capability, a density-based topology optimization framework is developed to optimize the spatial distribution of different materials, their interfaces, and the structural layout in order to enhance both the stiffness and the stress. Interpolation schemes to achieve these objectives are proposed, and the three levels of complexities, i.e., multi-material designs, design-dependent thermal loads, and stress constraints, are addressed. The framework is evaluated using three numerical examples, and the optimized stiffness and strength-based topology and material composition are demonstrated. Finally, the single-material and multi-material optimized designs are compared. The results show that the low compliance of the multi-material designs, while satisfying the failure constraint, was either infeasible or was achieved with a significantly higher weight for single-material structures.

1. Introduction

The advent of additive manufacturing (AM) has made it possible to fabricate the complex layouts designed by topology optimization [1–3]. It has also led to design optimizations for additive manufacturing in various fields, such as designing lightweight flight structures for space [4] and aviation [5,6] applications, reducing the sound radiation for acoustic applications [7], optimizing shapes for passive cooling [8], optimizing the fiber paths and topology of 3D-printed composites [9], and reducing stress-shielding in bio-implants [10]. An exceptional attribute of AM is implementing multiple materials in the fabrication of a unitized, single component [11]. One specific benefit of multi-material components is the ability to tailor the mechanical properties in various regions according to the desired functionality of the structure. For example, compliant inverters can be manufactured by utilizing stiff and flexible materials in the load transfer members and the hinge regions, respectively [12]. Another significant benefit of multi-material AM is that it can be used to create multi-functional structures by 3D printing components with different mechanical, thermal, electrical, and optical properties [13]. The development of multi-material AM began with polymers [14] and later included fiber-reinforced composites [15] and metals and alloys [16].

Despite the significant benefits of multi-material AM, there remain several issues that prevent its use for potential applications. One of the critical issues is the surface tension at the interface of two materials, which can cause cracks and delamination [17]. Fig. 1(a) shows the step-transition between two materials, in which one material is changed to the next in a transition layer. A possible solution for the interface issue is to create transition layers that do not have brittle phases [18].

Multi-material structures can also be found in various natural structures [19], and examining these structures has provided another solution for the interface issue. In multi-material natural structures, the changes between the various materials are gradual, and they occur through a gradient region [20]. This insight resulted in changing multi-material AM from the distribution of combinatorial material to a gradient methodology (Fig. 1(b)). By using gradient AM, a multi-functional structure can be printed that consists of regions with different materials as well as their graded compositions.

The significant advantages of gradient AM include: (1) the ability to create a smooth and gradual transition between different regions of the material, which reduces the concentration of stress and potential for failure resulting from mismatched materials

---

E-mail address: ali.tamijani@erau.edu

https://doi.org/10.1016/j.compstruc.2021.106641

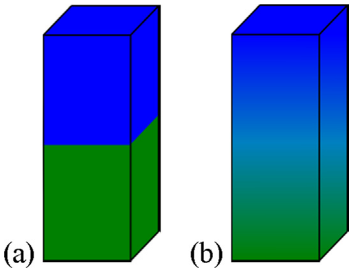

Fig. 1. Transition between two materials: (a) step transition, (b) smooth gradient [18].

[20,21], and (2) the capability of controlling the local deposition of the material and the graded composition, which results in tailored local mechanical or thermal properties and makes it possible to control the local physical properties, such as stress [22,23]. These gradient AM capabilities have been reported for using a Laser Deposition System to manufacture metal valves for automobiles. Finite element models of two sample valves were used, with one valve fabricated from 304L stainless steel and Inconel 625 with a 2.5 cm gradient transition, and one in which a friction weld was used to join the two regions of different materials [18]. The results showed a tenfold increase in the stress at the joint section of the friction-welded part compared to the graded transition part.

As discussed earlier, one of the main benefits of multi-material AM is its ability to distribute various materials in different parts of structures to enhance their functionality. This is where topology optimization offers a systematic procedure to design the material distribution to tailor the mechanical properties in various regions according to the desired functionality. The optimization of the topologies of multi-material structures started with research on the continuum topology optimization of multi-phase materials [24], the design of multi-physics actuators [25], and the design of microstructures with extreme thermal expansion [26]. With the advent of multi-material AM in recent years, topology optimization has been further developed for multi-material structures using various frameworks, e.g., solid isotropic material with penalization (SIMP), level set, bidirectional evolutionary structural optimization (BESO), and phase field [27]. In the SIMP framework, the Hashin-Shtrikman bounds [28] were studied for multiple-phase properties [29], a peak function was used for the design of multi-material compliant mechanisms [30], and the framework was extended into 3D for multi-material topology optimization [31]. Recently, isogeometric analysis has been used in conjunction with the density-based approach to perform topology optimization of functionally graded structures [32]. Phase-field methods have also been used to optimize the multi-material structures topologies by utilizing Cahn–Hilliard models [33,34]. In the framework of BESO, a material interpolation scheme was utilized for the topology optimization of multi-material structures. The results were compared with the results obtained using SIMP [35] and, later, were applied to the design of microstructures that consisted of multi-phase materials [36]. The BESO algorithm and a genetic algorithm also were used to determine the material property distribution of functionally graded structures [37]. In the level set framework, a color level set method [38] and a piecewise constant level set method [39] were developed for multi-material interpolation, and, later, the method was applied in the design of multi-material compliant mechanisms [40], piezoelectric actuators [41], and the heat conduction problem [42]. One of the issues with the multi-material level set approach is the sharp boundaries between the various phases. It has been shown that including the interface properties in the optimization procedure resulted in an enhanced, optimized design [43]. The effect of the interface properties on the optimization of multi-material structures also motivated the implementation of an extended finite element method and the use of a cohesive model in the level set approach to study the separation of the materials interfaces [44]. Another issue with multi-material optimization is that multiple level set functions overlap, resulting in redundant material phases. To address this issue, a multi-material level set method was developed by determining the property of the material in the design domain based on a combination rule of various level set functions, which prevented the phases from overlapping and removed the redundant regions [45].

While various aspects of the stiffness-based design of multi-material structures have been studied, higher stiffness will not be attained if failure occurs. In addition, considering the failure constraint in the optimization framework can change both the topology and the material composition of optimized structures. However, there are two main issues associated with including the stress constraints, even for a single-material, solid-void design, namely the singularity of the stress and the local nature of the stress constraints. The singularity of the stress occurs as the density converges to zero, which is due to a reduction of stiffness. To address this issue, various relaxation techniques, such as ε-relaxation [46], the qp-approach [47], and stress interpolation schemes [48], have been proposed to eliminate the low-density regions. The issue of a large number of constraints due to the local nature of stress also can be addressed by converting the local constraints to a single constraint or multiple global constraints using the Kresselmeier-Steinhauser [49] and p-norm and p-mean methods [50]. While the stress aggregation methods reduce the number of constraints, they do not fully represent the local stress behavior. To address this issue, clustering methods have been suggested [48,51], in which the design domain is divided into multiple regions based on the failure index level and then the failure indices of each region are aggregated into a single value. A challenge related to the clustering methods is identifying the appropriate number of clusters. Alternatively, the augmented Lagrangian method can be utilized to handle the local stress constraints in the density-based [52–54] and level set methods [55]. By using the augmented Lagrangian technique, the optimization problem with stress constraints is replaced with a sequence of optimization subproblems. The additional complexity of implementing stress constraints in the topology optimization of multi-material structures is the change in the allowable stress for the various material compositions. To handle the stress constraints in multi-material topology optimization, a heuristic approach based on discrete variables was proposed [56], but it has been reported that a critical limitation of this method is its inability to handle geometric stress singularities caused by re-entrant corners. A level set approach was also developed for the optimization of stress-constrained topology, and it has been shown how the optimized design could be different from the designs obtained based on engineering intuition [57]. The SIMP framework was extended to design compliant mechanisms with stress constraints, while the allowable stress was obtained based on the interpolation between the yield stress and Young's modulus of different materials [58].

As mentioned earlier, one of the main advantages of gradient AM techniques is their ability to control the local graded compositions and properties of the material, such as thermal expansion and Young's modulus. This capability can be used to reduce the displacement of a structure that is subjected to both mechanical and thermal loads. Topology optimization using the level set method has been utilized to design microstructures with graded interfaces for extreme thermoelastic properties [59]. Because thermal loads depend on the distribution of the material, the SIMP-based topology optimization of structures may generate undesirable intermediate density regions, even for a single-phase material. The appearance of low density in the optimized design mostly results from the zero sensitivity in those regions, which is remedied by using the Rational Approximation of Material Properties (RAMP) model [60]. Another issue in incorporating the thermal load is the appearance of the product between the thermal expansion coefficient and Young's modulus, in which the separate interpolation of these two properties increases the complexity of the problem. To simplify the relationships, the concept of the thermal stress coefficient (TSC) was introduced based on this product, and then a single TSC interpolation was proposed [61]. By using the RAMP interpolation and the TSC concept, a density-based topology optimization was developed for elastic strain energy minimization of multi-material structures [62]. The RAMP model and TSC concept were also utilized to study the multi-material topology optimization of thermo-mechanical buckling problems [63]. Recently, a B-spline multi-parameterization method based on the RAMP model and TSC was developed for thermoelastic structures topology optimization [64], and a multi-material thermomechanical topology optimization method was developed to design support structures for AM [65].

The goal of the current work is to use the capability of gradient AM to control the local mechanical properties and develop a density-based optimization framework that simultaneously optimizes the structural layout and the material composition of the structure to withstand thermal and mechanical stresses and deformation. The three major contributions of this work are: (1) the derivation of five interpolation schemes that satisfy the requirements of obtaining solid-void designs with distinct regions of various materials and obtaining interface properties that satisfy the variational bounds, (2) the incorporation of the failure constraint and its related sensitivity analysis in the optimization scheme of multi-material designs, and (3) an evaluation of the framework for three benchmark numerical examples and the demonstration of its capability to utilize the superior properties offered by each material to obtain stiffness and strength values that are infeasible in single-material designs. In the following sections, the material interpolation schemes, finite element models, sensitivity analysis, density filtering, and optimization problem statements are presented, and the effectiveness of the developed framework is demonstrated using numerical examples.

2. Formulation of the problem

The formulation for a density based-topology optimization problem to minimize the mass subjected to compliance and strength constraints is discussed in this section. Consider a 2D continuum structure (D) that consists of three phases (material A, material B, and void) subjected to a traction (f_A) on the ∂D_Acurve and supported on the ∂D_Rcurve, as shown in Fig. 2. The goal of the proposed framework is the concurrent optimization of the topology (solid-void) and the distribution of two materials in the solid region. Therefore, the design variables are: (1) the distribution of solid ($x_1 \in (0,1]$) in the design domain, and (2) the amount of materials A and B in the solid regions ($x_2 \in [0,1], (1-x_2)$). This section presents the various interpolation schemes, the finite element formulation and corresponding stiffness matrix and force vectors, the filtering of design variables, and the derivation of the failure criterion. Subsequently, the optimization formulation and related sensitivity analysis are discussed.

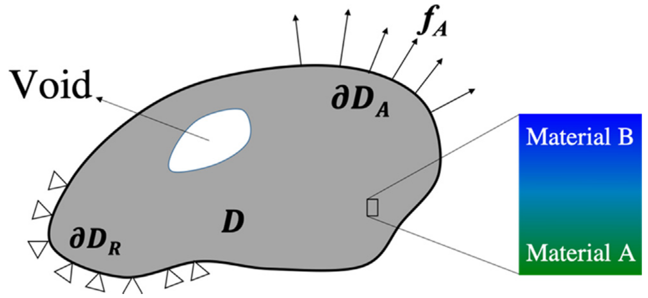

Fig. 2. Continuum structure model.

2.1. Material interpolation and finite element models

The RAMP model is used in the proposed material interpolations because it is more effective for problems with a design-dependent load, such as a thermal load. The RAMP model is in the form of $P = P_2 + \frac{x}{1+q(1-x)}(P_1 - P_2)$ [66], where P_i is the property of the i^th phase, and q is the RAMP parameter. The RAMP and SIMP (x^p) interpolations are compared in Fig. 3. As can be seen, the SIMP model ($p = 3.0$) has zero derivative at zero density. Other research has shown that the insensitivity at low density causes numerical difficulties for density-dependent mechanical [67] and thermal loads [60,61]. This issue is fixed in the RAMP model (see Fig. 3, $q = 8.0$).

For $q \gg 1$, the RAMP interpolation is concave up, which means the property is lower than a linear interpolation for the intermediate densities. Another region of q also considered in this work, i.e., $-1 < q < 0$, has a concave down interpolation, i.e., the property is higher than a linear interpolation for the intermediate densities. Fig. 3 shows the interpolation ($\eta = \frac{x}{1+q(1-x)}$) for the RAMP parameters in the two regions mentioned above. As can be seen in Fig. 3, the RAMP and SIMP interpolations with $q = -0.7$ and $p = 0.5$ are close to each other. The concave down SIMP model with $p = 0.5$, which results in higher stresses for the intermediate densities, has been previously shown to be effective in obtaining a stress-constrained solid-void design [48]. Five interpolation schemes are introduced based on the RAMP model in this work, i.e., the mass (η^M), stiffness (η^E), thermal stress coefficient (η^β), allowable stress (η^σ), and failure criterion (η^F) interpolations. The interpolation schemes are developed such that: (1) the intermediate densities are penalized to obtain a solid-void design (x_1 converges to zero or one), (2) mixing the materials is avoided except at the interface of the two materials where the composition changes gradually, and (3) the properties of the material at the interface satisfy the Hashin-Shtrikman bounds [28]. As shown in [16], the reason for avoiding the mixture of materials is that the low thermal expansion of Invar (the material considered in this research) vanishes for the intermediate composition with 304L stainless steel, which has a high thermal expansion (304L is another material considered in this research).

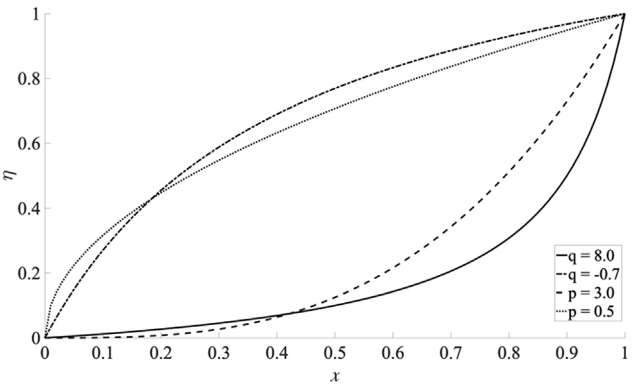

Fig. 3. RAMP and SIMP models.

The first interpolation is developed for mass. The total mass can be written as:

$$M = \int_D x_1\left(\rho^B + x_2\left(\rho^A - \rho^B\right)\right)dv \tag{1}$$

where ρ is the density for materials A and B. Therefore, η_1^m and η_2^m are:

$$\eta_1^m = x_1 \text{ and } \eta_2^m = x_2\,; M = \int_D \eta_1^m\left(\rho_B + \eta_2^m\left(\rho^A - \rho^B\right)\right)dv \tag{2}$$

Therefore, $q = 0$ for the mass interpolations. For the stiffness, η_1^E and η_2^E are introduced, and the interpolated Young's modulus is written as:

$$\begin{aligned}&E(x_1, x_2) = \eta_1^E\left(E_B + \eta_2^E\left(E_A - E^B\right)\right);\\&\eta_1^E = \frac{x_1}{1+q_1^E\left(1-x_1\right)} \text{ and } \eta_2^E = \frac{x_2}{1+q_2^E\left(1-x_2\right)}\end{aligned} \tag{3}$$

where E is Young's modulus. In this research it is assumed that $(E^A \geq E^B)$. In order to penalize the stiffness and obtain a solid-void design, q_1^E is selected to be a positive large number ($q_1^E = 8$ in this work). Also, to ensure that the Young's modulus that corresponds to the material composition in the solid region satisfies the Hashin-Shtrikman bounds, q_2^E is taken such that $\frac{2}{3}\frac{\left(E^A - E^B\right)}{E^B} \leq q_2^E \leq \frac{2\left(E^A - E^B\right)}{\left(E^A - 2E^B\right)}$ (for materials with Poisson's ratio equal to 1/3 [66]). In this research, the q_2^E that corresponded to the lower bound ($q_2^E = \frac{2}{3}\frac{\left(E^A - E^B\right)}{E^B}$) was selected to penalize the mixture of materials.

For the allowable stress, η^σ was introduced, where q^σ is chosen with the same form as q_2^E with Young's modulus replaced by allowable stress for two materials. The interpolated allowable stress (σ_a) is established as:

$$\sigma_a\left(x_2\right) = \sigma_a^B + \eta^\sigma\left(\sigma_a^A - \sigma_a^B\right); \eta^\sigma = \frac{x_1}{1 + q^\sigma\left(1 - x_2\right)} \tag{4}$$

The product between the thermal expansion coefficient (α) and Young's modulus, which appears in the thermal load, is defined as the thermal stress coefficient (TSC; $\beta = E\alpha$ [62]). For the TSC, η_1^β and η_2^β are introduced, and the interpolated TSC can be written as:

$$\begin{aligned}&\beta(x_1, x_2) = \eta_1^\beta\left(\beta^B + \eta_2^\beta\left(\beta^A - \beta^B\right)\right);\\&\eta_1^\beta = \frac{x_1}{1+q_1^\beta(1-x_1)} \text{ and } \eta_2^\beta = \frac{x_2}{1+q_2^\beta(1-x_2)}\end{aligned} \tag{5}$$

To further penalize the thermal load (obtain a higher thermal load compared to the stiffness for intermediate densities), $q_1^\beta$is selected such that $q_1^\beta < q_1^E$ ($q_1^\beta = 4$ in this work). It has been shown in experimental tests of graded materials that the thermal expansion is concave down for the intermediate densities [16]; therefore, $q_2^\beta$is selected to be equal to the negative value of q_2^E. Note that both q^σ and q_2^β can be changed in the developed framework based on the experimental data of various material compositions.

The von Mises stress (σ_{vm}) is used in this work to predict the failure in the structure [68]:

$$\sigma_{vm} = \sqrt{\sigma_x^2 + \sigma_y^2 - \sigma_x\sigma_y + 3\tau_{xy}^2} \tag{6}$$

where σ_x, σ_y, and τ_{xy} are the normal and shear stress components of the element stress tensor ($\boldsymbol{\sigma_e}$). A concave down failure criterion interpolation (η^F) is proposed to address the stress singularity issue and penalize the intermediate x_1 design variable ($q^F = -0.7$ in this work). By using the η^F interpolation, the relaxed von Mises stress can be written as:

$$\sigma_{vm}^r(x_1) = \eta^F\sigma_{vm}; \eta^F = \frac{x_1}{1 + q^F(1 - x_1)} \tag{7}$$

The element relaxed von Mises stress is then normalized with respect to the interpolated allowable stress ($\frac{\sigma_{vm,e}^r}{\sigma_{ae}}$), and they are aggregated to a single constraint value using the p-mean function (F^P) [48]:

$$F^P = \left(\left(\frac{1}{ne}\right)\sum_{e\in D}\left(\frac{\sigma_{vm,e}^r}{\sigma_{ae}}\right)^p\right)^{\frac{1}{p}} \tag{8}$$

where ne is the number of elements in design domain D, and p is a tuning coefficient. (See [48,50] for a detailed discussion of the p-norm and p-mean functions.) In this research, the p-mean coefficient is taken as $p = 10$. When the optimization converges, the p-mean function also converges to a constant value that is lower than the maximum value of ($\frac{\sigma_{vm,e}^r}{\sigma_{ae}}$). Therefore, an adaptive scaling factor (s) for each iteration (k) is implemented in the p-mean approximation to bring it closer to the maximum value of ($\frac{\sigma_{vm,e}^r}{\sigma_{ae}}$) [48]:

$$\begin{aligned}&F^P = s^k\left(\left(\frac{1}{ne}\right)\sum_{e\in D}\left(\frac{\sigma_{vm,e}^r}{\sigma_{ae}}\right)^p\right)^{\frac{1}{p}};\\&s^k = \alpha^k\frac{\max\left(\frac{\sigma_{vm,e}^r}{\sigma_{ae}}\right)^{k-1}}{\left(F^P\right)^{k-1}} + (1 - \alpha^k)s^{k-1}\end{aligned} \tag{9}$$

where $\alpha^k = 0.5$ if s is oscillating between two consecutive iterations; otherwise, $\alpha^k = 1.0$.

A finite element model (FEM) that consisted of four node elements with nodal displacements (u_0 and v_0) was chosen to discretize and analyze the design domain (D). The linear static FEM equation can be written as:

$$\boldsymbol{K}(\boldsymbol{x}_1, \boldsymbol{x}_2)\boldsymbol{U}(\boldsymbol{x}_1, \boldsymbol{x}_2) = \boldsymbol{F}(\boldsymbol{x}_1, \boldsymbol{x}_2) \tag{10}$$

where $\boldsymbol{K}$, $\boldsymbol{U}$, and $\boldsymbol{F}$ are the stiffness matrix, the displacement vector, and the force vector, respectively, and the $\boldsymbol{x}_1$ and $\boldsymbol{x_2}$ vectors consist of design variables x_1 and x_2 for each element. The force vector includes both the mechanical loads, $\boldsymbol{F^m}$, which are considered to be design independent, and the design-dependent thermal loads $\boldsymbol{F^{th}}(\boldsymbol{x}_1, \boldsymbol{x}_2)$. The stiffness matrix and thermal loads vector are assembled by the summation of element stiffness ($\boldsymbol{k_e}$) and the nodal load vector ($\boldsymbol{f_e^{th}}$) [60]:

$$\boldsymbol{k_e}(x_1, x_2) = E(x_1, x_2)\int_{\boldsymbol{D_e}} \boldsymbol{B_e^T}\bar{\boldsymbol{C}}\,\boldsymbol{B_e}\boldsymbol{dv}$$

$$\boldsymbol{f_e^{th}}(x_1, x_2) = \beta(x_1, x_2)\int_{\boldsymbol{D_e}} \boldsymbol{B_e^T}\,\bar{\boldsymbol{C}}\,\Delta T_e\Phi^{\boldsymbol{T}}\boldsymbol{dv} \tag{11}$$

where $\boldsymbol{B_e}$ is the element strain–displacement matrix, $\bar{\boldsymbol{C}}$ is a matrix that consists of the design-independent terms of the constitutive matrix, ΔT_e is the change in the temperature of the element, and $\boldsymbol{\Phi}$ for the two-dimensional problem is the $[1\ 1\ 0]$ vector. The stresses are computed at the center of element based on the displacement from FEM analysis [60]:

$$\boldsymbol{\sigma_e} = \bar{E}\,\bar{\boldsymbol{C}}\,\boldsymbol{B_e}\boldsymbol{U_e} - \bar{\beta}\,\bar{\boldsymbol{C}}\,\boldsymbol{\Phi^T}\boldsymbol{\Delta T_e} \tag{12}$$

where $\bar{E} = E_B + \eta_2^E(E_A - E_B)$ and $\bar{\beta} = \beta_B + \eta_2^\beta(\beta_A - \beta_B)$ are the Young's modulus and the TSC of the material composition in the solid region, respectively.

2.2. Filtering of the design variable

A weighted decaying filtering [69] is used in the proposed framework to address the checkerboard and mesh-dependency issues:

$$\tilde{x}_{ie} = \frac{1}{\sum_{j\in N_e} H^i_{ej}} \sum_{j\in N_e} H^i_{ej} x_{ij}$$

$$H^i_{ej} = \max(0, r_i - \Delta(e,j)) \tag{13}$$

where $\tilde{\boldsymbol{x}}_i$ is the filtered design variable, $i \in (1,2)$, N_e is the set of design variables x_{ij} with the distance to design variable x_{ie} $(\Delta(e,j))$ smaller than the radius r_i, and H^i_{ej} is the weighting decaying function. By using a chain rule, the sensitivity of a function f is transformed from a filtered variable to the design variable:

$$\frac{\partial f}{\partial x_{ie}} = \sum_{j\in D} \frac{\partial f}{\partial \tilde{x}_{ij}} \frac{\partial \tilde{x}_{ij}}{\partial x_{ie}} \tag{14}$$

Eqs. (13) and (14) show that the design variables x_1 and x_2 are filtered separately using different radii (r_i). In this research $r_2 = 1.5r_1$, to ensure that there is sufficient feature thickness for the fabrication of two materials, and r_1 is double the element size for all of the test cases studied here.

2.3. Optimization problem statements

Two optimization problems are considered in this research: (1) minimizing the compliance (SE) subjected to the equilibrium equation and mass constraint $(\overline{\mathrm{M}})$, and (2) minimizing the mass (M) subjected to the equilibrium equation, compliance $(\overline{SE})$, and the failure constraints. As mentioned earlier, one of the goals in this work is to avoid the mixture of different materials, except at the interface of two materials where the composition changes gradually. Motivated by the penalty function used in [62], an adaptive function is added to the objective function to penalize the material mixture:

$$f_2 = \left(cf \ /f_2^{\,0}\right) \int_D \boldsymbol{x}_1 \boldsymbol{x}_2 (1 - \boldsymbol{x}_2) dv \tag{16}$$

where cf is a weight that gradually increases from 0.001 to 0.1 in 100 iterations and then remains constant, and $f_2^{\,0}$ is the initial value of f_2 ($f_2^0 = \int_D x_1 x_2 (1 - x_2) dv$ in the first iteration). The reason for the gradual increase in the weight of the mixture $(cf\ )$ in the objective function is to prevent its influence in the early iterations and slowly increase it to converge to a distinct, multi-material design. Therefore, the optimization problem of minimizing the compliance subjected to the equilibrium equation and the mass constraint (g_1) can be written as:

$$\begin{gathered} \min \tfrac{SE}{SE_0} + f_2 \\ \text{subjected} \quad \text{to} \begin{cases} \boldsymbol{KU} = \mathbf{F} \\ g_1 = \frac{\mathrm{M}}{\overline{\mathrm{M}}} - 1 \le 0 \end{cases} \\ \text{design} \quad \text{variables} \quad 0 < x_{ie} \le 1.\ i = 1,2 \quad \text{and} \quad e = 1,2,\cdots,ne \end{gathered} \tag{17}$$

where $SE = \boldsymbol{UKU}$, SE_0 is the initial value of SE, and $\overline{M}$ is the upper bound of the mass. The second optimization problem considered here is minimizing the mass subjected to the equilibrium equation, compliance (g_1), and stress (g_2) constraints:

$$\begin{gathered} \min \tfrac{M}{M_0} + f_2 \\ \text{subjected} \quad \text{to} \begin{cases} \boldsymbol{KU} = \mathbf{F} \\ g_1 = \frac{\mathrm{SE}}{\overline{\mathrm{SE}}} - 1 \le 0 \\ g_2 = F^P - 1 \le 0 \end{cases} \\ \text{design} \quad \text{variables} \quad 0 < x_{ie} \le 1.\ i = 1,2 \quad \text{and} \quad e = 1,2,\cdots,ne \end{gathered} \tag{18}$$

where M_0 is the initial value of mass, and $\overline{SE}$ is the upper bound of compliance. Both optimization problems are solved using the globally convergent method of moving asymptotes (GCMMA) [70]. To control the changes in the design variable in each iteration, an adaptive move limit is implemented within the GCMMA scheme. The proposed adaptive move limit is based on the behavior of the objective and the constraint functions in each iteration. If there is an oscillation of the objective or the constraint functions between two consecutive iterations, then the move limit is decreased by 25%; if there is no oscillation but the constraints are not satisfied, then the move limit is kept unchanged. Finally, if there is no oscillation of the objective or constraint functions and the constraint is satisfied, then the move limit is increased by 25%, considering the maximum move limit of 0.5.

2.4. Sensitivity analysis

The sensitivity analysis is provided to GCMMA to determine the changes in the design variables in each optimization iteration. First, the sensitivity of compliance is obtained using an adjoint method [61]:

$$\boldsymbol{\frac{dSE}{dx_{ie}}} = -\boldsymbol{U^T} \boldsymbol{\frac{dK}{dx_{ie}}} \boldsymbol{U} + 2\boldsymbol{U^T} \boldsymbol{\frac{dF^{th}}{dx_{ie}}} \tag{19}$$

The sensitivity of the failure criterion is also required for the optimization problem (18). The sensitivity analysis of the p-mean function for a multi-material structure is more complicated than compliance, since (a) it is not self-adjoint, (b) the dependency on density (x_1) and material composition (x_2) appears in different parts of the p-mean function, and (c) the allowable stress is also a function of the material composition. Therefore, the sensitivity equations are derived separately for x_1 and x_2 (see Appendix for additional details of the sensitivity analysis):

$$\frac{dF^P}{dx_{1e}} = \frac{\left(F^P\right)^{1-p}}{ne} \frac{\sigma_{vm,e}}{\sigma_{ae}} \left(\frac{\sigma^r_{vm,e}}{\sigma_{ae}}\right)^{p-1} \frac{d\eta^F_e}{dx_{1e}} + \boldsymbol{\lambda}^{\boldsymbol{T}}_{\boldsymbol{\sigma}} \left(\frac{d\boldsymbol{F^{th}}}{dx_{1e}} - \frac{d\boldsymbol{K}}{dx_{1e}}\boldsymbol{U}\right)$$

$$\begin{aligned} \frac{dF^P}{dx_{2e}} &= \frac{\left(F^P\right)^{1-p}}{ne} \frac{\eta^F_e}{\sigma_{ae}} \left(\frac{\sigma^r_{vm,e}}{\sigma_{ae}}\right)^{p-1} \\ &\quad \times \frac{d\sigma_{vm,e}}{d\boldsymbol{\sigma_e}} \left(\frac{d\bar{E}_e}{dx_{2e}} \bar{\mathbf{C}} \boldsymbol{B_e U_e} - \frac{d\bar{\beta}_e}{dx_{2e}} \bar{\mathbf{C}}\, \Phi^{\mathbf{T}} \Delta T_e\right) - \frac{\left(F^P\right)^{1-p}}{ne} \\ &\quad \times \frac{1}{\sigma_{ae}} \left(\frac{\sigma^r_{vm,e}}{\sigma_{ae}}\right)^{p} \frac{d\sigma_{ae}}{dx_{2e}} + \boldsymbol{\lambda}^{\boldsymbol{T}}_{\boldsymbol{\sigma}} \left(\frac{d\boldsymbol{F^{th}}}{dx_{2e}} - \frac{d\boldsymbol{K}}{dx_{2e}}\boldsymbol{U}\right) \end{aligned} \tag{20}$$

where λ^T_σ is calculated using Eq. (21):

$$\boldsymbol{\lambda}^{\mathbf{T}}_{\boldsymbol{\sigma}} \boldsymbol{K} = \sum_{e\in Ne} \frac{\left(F^P\right)^{1-p}}{ne} \frac{\eta^F_e}{\sigma_{ae}} \left(\frac{\sigma^r_{vm,e}}{\sigma_{ae}}\right)^{p-1} \frac{d\sigma_{vm,e}}{d\boldsymbol{\sigma_e}} \bar{E}_e \bar{\mathbf{C}} \boldsymbol{B_e} \frac{\mathbf{dU_e}}{\mathbf{dU}} \tag{21}$$

3. Results and discussion

In this section, the proposed density-based multi-material topology and composition optimization framework are evaluated for three well-known cases in topology optimization for mechanical and thermal loads. For each case, the compliance-based optimization is performed first for the multi-material and single-material design domains. Then, the optimized compliance is taken as a constraint in a mass minimization that also includes a failure constraint. The penalization parameters for stiffness (η_1^E), the thermal stress coefficient (η_1^β), and the failure criterion (η_1^F) are gradually increased in 15 iterations to avoid convergence to a suboptimal solution [71]. In order to show the two-material design, the final design variables are interpolated onto a finer mesh (5 times the number of elements in each test case). The two materials considered for all of the test cases in this research are stainless steel 304L (Material A) and Invar 36 (Material B). In all of the test cases in this research, the green and blue colors show the distributions of the 304L and Invar 36 materials, respectively. The density for both materials is 8100kg/m^3, and the Poisson's ratio is 1/3. The elastic modulus and thermal expansion coefficient of the 3D printed Invar 36 and 304L and the yield strength of the 3D printed 304L are based on the experimental data in [16,72]. The yield strength for Invar 36 is based on data available in [73]. The properties of stainless steel 304L and Invar 36 are shown in Table 1.

Table 1 shows that Invar 36 has a lower thermal expansion coefficient, so it is very suitable for thermal loads. However, the 304L material has a higher stiffness and higher allowable stress, which make it preferable for mechanical loads and regions subjected to high stress. Depending on the boundary conditions, some non-designable regions are considered for each test case. For the cases in which multiple materials are used in the design, the non-designable regions are made of 304L. For the single-material design cases, the non-designable regions are made of the same material. The von Mises stress is normalized by the allowable stress (Eq. (4)) and it is shown for all the test cases.

3.1. Cantilever plate

The first test case is a plate with a rectangular cross section, clamped at the left edge, subjected to a shear force $R = 70kN$ at its right edge. Also, a uniform elevated temperature of $\Delta T = 30^\circ C$ is considered. The width, height, and thickness of the plate are $2L = 80cm$, $L = 40cm$, and $t = 1cm$, respectively. The plate is discretized using 12,800 plane stress elements. Two regions consisting of 5×10 elements in the neighborhood of the load and 4×80 elements on the left edges are excluded from the design domain. The non-designable regions (shown in black) and the boundary conditions are depicted in Fig. 4. The compliance-based optimization (17) is performed for the multi-material design domain with $\overline{M} = 10kg$. Fig. 5(a) shows the optimized topology, distribution of the two materials, and compliance ($SE = 197Nm$). Fig. 5(b) shows the interface between 304L and Invar 36 (the transition from A to B in Fig. 5(a)). The principle stresses in the optimized design also are shown in Fig. 5(c) and (d). It is apparent that the advantages provided by each material are used to create a structure with high stiffness; the material with higher stiffness and thermal expansion (304L) is located in the compression region to reduce the displacement, and the material with lower thermal expansion (Invar 36) is distributed in the tension region. This configuration can also be explained by the principle stresses shown in Fig. 5(c) and (d), where 304L is distributed in the region with negative principle stresse, and Invar 36 is located in the region with positive principle stress.

Table 1
Material Properties of Stainless Steel 304L and Invar 36.

Properties	Stainless Steel 304L	Invar 36
Elastic Modulus, $E(GPa)$ [16]	240	160
Coefficient of Thermal Expansion, $\alpha(10^{-6}/^\circ C)$ [16]	15	1.5
Allowable Stress, $\sigma_a(MPa)$ [72,73]	400	275

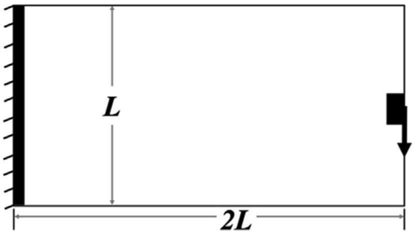

Fig. 4. Cantilever Plate with a point load applied at the free edge.

Next, the compliance optimization is performed for the single-material design domain, i.e., Invar 36 and then 304L. The optimization formulation is changed slightly to provide a better comparison between the multi-material design and the single-material design. In the case of Invar, the weight is minimized, taking into consideration a compliance constraint equal to the optimized compliance for the multi-material design ($\overline{SE} = 197Nm$). Fig. 6(a) shows the optimized topology for Invar with the optimized mass of $M = 12.5kg$, which is 25% higher than the resources required for the multi-material design to obtain the same compliance. In the case of the 304L material, with its high thermal expansion, regardless of the amount of material used, the optimization can never reach the multi-material compliance level. The optimized compliance for the 304L design domain is $SE = 322.3Nm$, and the corresponding mass is $M = 11.6kg$. (See Fig. 6(b).) The optimization problem for the 304L material becomes unconstrained if it is performed with a mass constraint greater than $M = 11.6kg$, which means that adding more material will only make the compliance higher. The comparison of Fig. 6(a) and (b) also shows that, while the optimized topology for the Invar is similar to that obtained for only mechanical loads due to its low thermal expansion [74], more support is required for the tension region located on the top of the domain for the 304L case.

Though the multi-material design domain compliance is optimized, the failure constraint has yet to be considered. As a result, the von Mises stress was 50% higher than the allowable stress. (See Fig. 7.) To address this issue, the optimization problem (18) is studied to include the failure constraint as well as the compliance constraint. The upper bound of compliance is taken as the optimized compliance of the multi-material design ($\overline{SE} = 197Nm$). Fig. 8 shows the optimized configuration, mass, and normalized von Mises stress for the optimized design. The optimized topology is similar to the compliance-based design, but there is a slight change in the optimized distribution of the material. The von Mises stress for optimized compliance in Fig. 7 makes it clear that 304L, with its higher allowable stress, is distributed in the top left corner and middle regions to alleviate the higher stresses in these areas. By using the higher allowable stress of 304L and distributing it in the high stress regions while using the Invar 36 in the compression region, both the compliance and the failure constraints are satisfied by an increase in resources of only 5% ($M = 10.5kg$) compared to the optimized compliance design. The comparison of the two von Mises stresses for the optimization problems without failure constraints (Fig. 7) and with failure

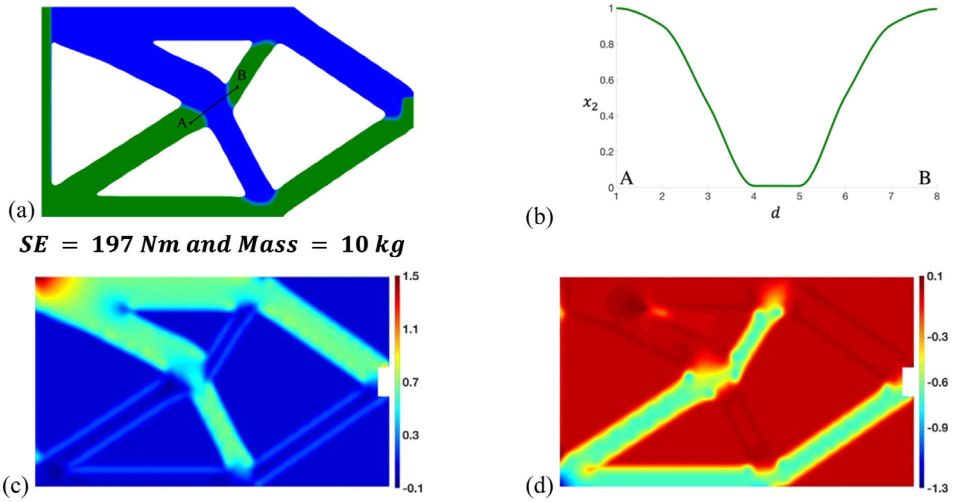

$SE = 197\ Nm\ and\ Mass = 10\ kg$

Fig. 5. Compliance-based design for the cantilever plate; (a) The topology and material distribution; (b) the transition between 304L and Invar 36 A-B; (c) and (d) are principle stresses.

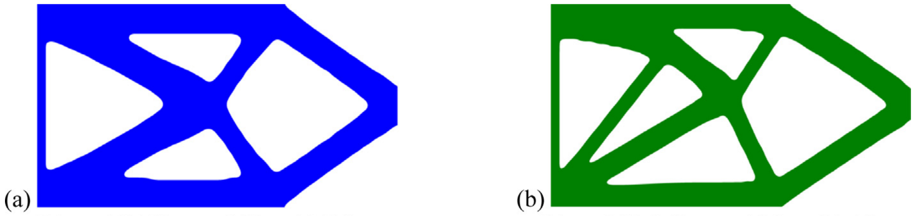

$SE = 197\ Nm\ and\ M = 12.5\ kg$ $SE = 322.3\ Nm\ and\ M = 11.6\ kg$

Fig. 6. Compliance-based designs for a cantilever plate with (a) Invar 36 and (b) 304L.

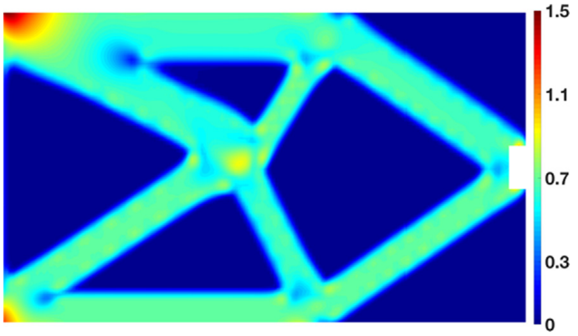

Fig. 7. The von Mises stress normalized by the allowable stress for multi-material optimized compliance design.

constraints (Fig. 8(b)) shows the more effective distribution of stress for the optimization with the stress constraint. The optimization problem with failure and compliance constraints can only be performed for Invar 36, however, because 304L cannot reach the required $\bar{SE}$. Figure 9 shows the optimized topology for the Invar material. The optimized mass in this case is $M = 15.4kg$, which is about 50% higher than the multi-material design. It is worth noting that satisfying the failure constraint in addition to the compliance constraint resulted in a 25% increase in the weight for the structure made of Invar 36.

3.2. L-bracket

The second numerical example is an L-shaped bracket, which is a well-known case study for optimization with failure constraints due to the geometric stress singularity caused by the re-entrant corner. The dimensions and boundary conditions, including the clamped top edge and a point load applied on the right corner ($R = 22kN$) are shown in Fig. 10. The thickness is $1cm$. The structure is under a uniform, elevated temperature of $\Delta T = 30^{\circ}C$. The domain is discretized using 6400 plane stress elements. A region

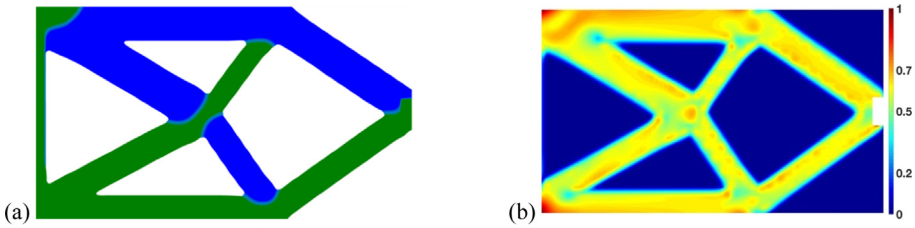

$M = 10.5\ kg$

Fig. 8. Cantilever plate optimization results with failure and compliance constraints: (a) topology and material distribution; (b) normalized von Mises stress.

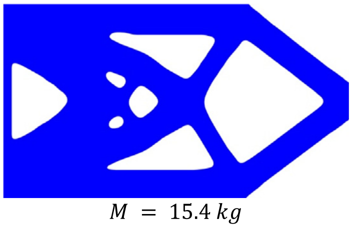

Fig. 9. Optimized topology with failure and compliance constraints for a cantilever plate made of Invar 36.

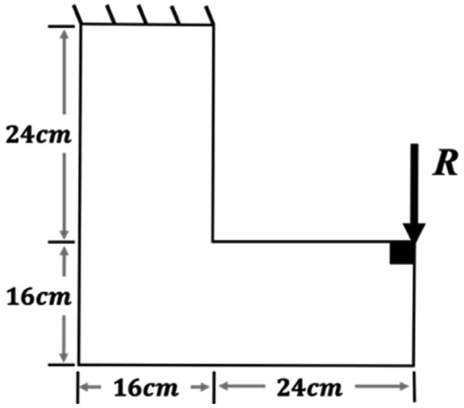

Fig. 10. L-bracket design domain.

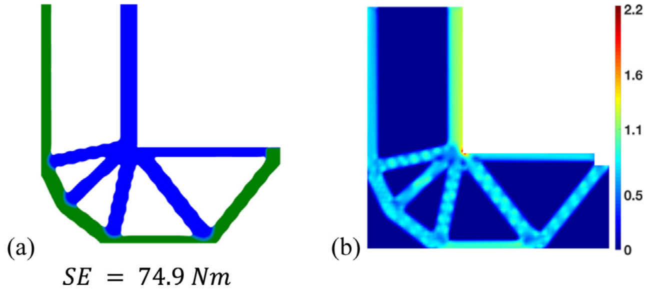

Fig. 11. L-bracket compliance design: (a) optimized topology and material distribution; (b) normalized von Mises stress.

that consists of 5×5 elements under the load is excluded from the design domain. First, the compliance-based optimization problem (17) is studied for the multi-material design domain with a mass constraint of $\overline{M} = 2.5kg$. The optimized topology and material distribution and optimized compliance ($SE = 74.9Nm$) are shown in Fig. 11(a). Figure 11(b) shows the normalized von Mises stress, which is twice the allowable stress. Next, the mass minimization subjected to the compliance constraint ($\overline{SE} = 74.9Nm$) is performed for the single-material design domain (Invar 36 or 304L). Fig. 12(a) shows the optimized topology for the Invar 36 design domain, and the corresponding optimized mass is $M = 3.1kg$, which is 24% higher than the two-material design. For the 304L design, the targeted compliance could not be reached irrespective of the amount of material; the optimized compliance is $SE = 104Nm$, and the corresponding mass M is $3kg$ (Fig. 12(b)). The stiffness-based optimized topology for both materials is similar to those obtained when subjected to mechanical load [58].

Fig. 11(b) shows that the failure constraint is not satisfied, which is due mostly to the stress concentration at the right-angle corner of the design. Therefore, the failure constraint is added to the optimization formulation along with the compliance constraint ($\overline{SE} = 74.9Nm$) according to the optimization statement (18). The optimized topology and composition of the material and the normalized von Mises stress are shown in Fig. 13(a) and (b), respectively. The optimized mass is $M = 3.3kg$. Due to its higher allowable stress, the 304L is located in the high stress region, and Invar 36, with its lower thermal expansion, is located in the tension region. Also, 304L, with its higher Young's modulus, is distributed in the region being subjected to compression. Figure 13(b) also shows that the right-angle corner is changed to a curved member so that the failure constraint is satisfied. The effect of mesh refinement on optimized topology and two material distribution is investigated, and the results are shown in Fig. 14. The comparison of the optimized designs presented in Fig. 13 and Fig. 14 shows that the mesh refinement did not yield significant changes in optimized topology and material distribution. The optimized stress-based topology is also similar to those reported for mechanical and thermal loads [48,60]. However, the stress distribution is not completely uniform due to the fact that the compliance constraint must also be satisfied. If the compliance constraint were to be relaxed by 30% ($\overline{SE} = 1.3 \times 74.9Nm$), then both the material and the stress distributions would be changed, and a design with more uniform stress would be obtained (see Fig. 15). Now, the 304L material is occupying a larger region because, in this case, the failure is a more critical constraint, and the Invar material is distributed in the middle to reduce the load on the high stress region above it.

For the L-bracket test case, optimization with a single material cannot reach the targeted compliance while satisfying the failure constraint. The Invar 36 design cannot satisfy the failure constraint, and the 304L cannot attain the stiffness of the multi-material design. Therefore, with an optimized, multi-material L-bracket, a level of performance can be achieved that would be impossible with a single-material design, irrespective of the amount of resources.

Fig. 12. Compliance-based designs for the L-bracket with (a) Invar 36 and (b) 304L.

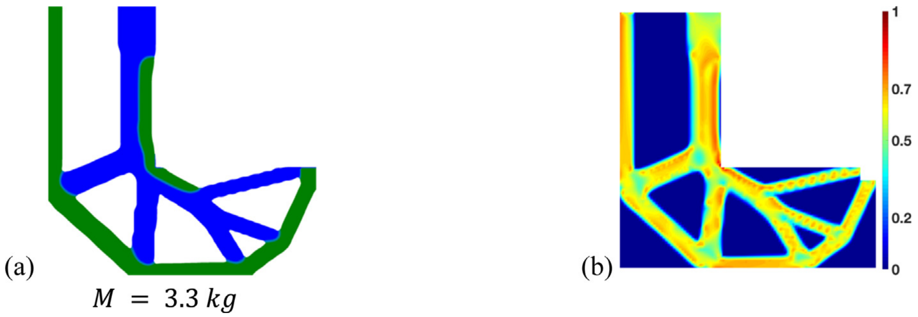

Fig. 13. L-bracket optimization results with failure and compliance constraints: (a) topology and material distribution; (b) normalized von Mises stress.

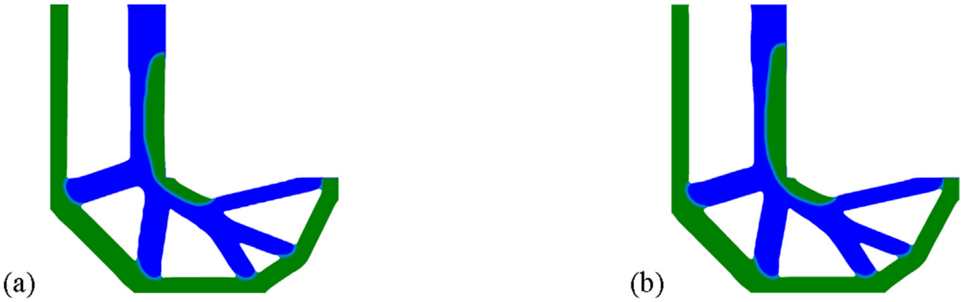

Fig. 14. L-bracket optimization results with failure and compliance constraints with two levels of mesh refinement: (a) 12,800 elements; (b) 25,600 elements.

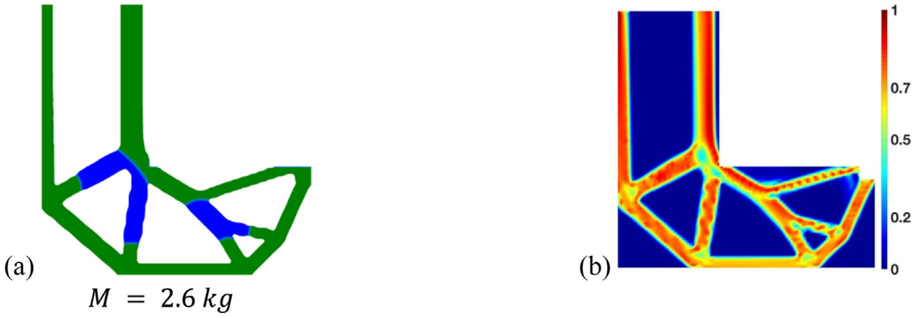

Fig. 15. L-bracket optimization results with failure and relaxed compliance constraints: (a) topology and material distribution; (b) normalized von Mises stress.

3.3. Bi-clamped plate

The last numerical example is a plate clamped on both the right and left sides, which is a popular test case for topology optimization for both mechanical ($R = 220kN$) and thermal loads ($\Delta T = 30^{\circ}C$). Figure 16 shows the dimensions and boundary conditions. The thickness of the plate, t, is $1cm$. The domain is discretized using 9600 plane stress elements. The two regions consisting of 6 × 12 elements under the load and 2 × 80 elements on the right and left edges are excluded from the design domain (shown in black in Fig. 16). The compliance-based optimization is performed using the multi-material design domain with a mass constraint, $\bar{M} = 6kg$. Figure 17 shows the optimized topology, material distribution, compliance ($SE = 139.5Nm$), and the normalized von Mises stress. Similar to previous test cases, 304L is located in the region subjected to compression, and Invar 36 is distributed in the tension region to reduce the deformation. However, the von Mises stress is 40% higher than allowable stress. The compliance-based multi-material design (Fig. 17 (a)) is in agreement with those reported in [62]. The mass minimization with the compliance constraint ($\bar{SE} = 139.5Nm$) is performed for the single-material design domain. Figure 18 (a) shows the optimized topology for the Invar 36 design domain, and the corresponding optimized mass, M, is $6.5kg$, which is 8% higher than the two-material design. Similar to the previous 304L material cases, the compliance of $\bar{SE} = 139.5Nm$ cannot be obtained (Fig. 18(b)). The optimized compliance is $SE = 162.9Nm$,and the corresponding mass, M, is $7.6kg$. It is interesting to see the difference between the topologies of the multiple material design and the Invar 36 design. While it is advantageous to include the compression region in the multi-material

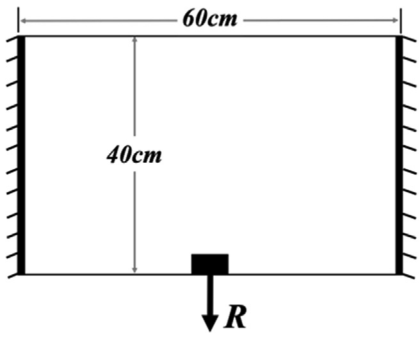

Fig. 16. Bi-clamped plate design domain.

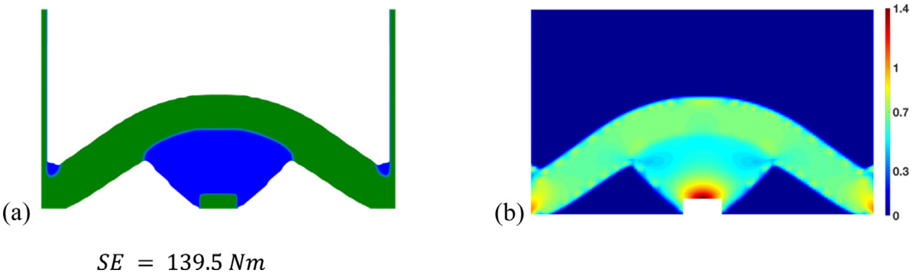

Fig. 17. Bi-clamped compliance design: (a) optimized topology and material distribution; (b) normalized von Mises stress.

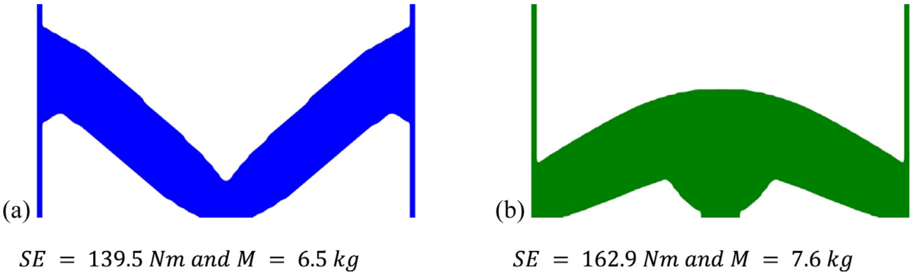

Fig. 18. Compliance-based designs for a bi-clamped plate: (a) with Invar 36; (b) with 304L.

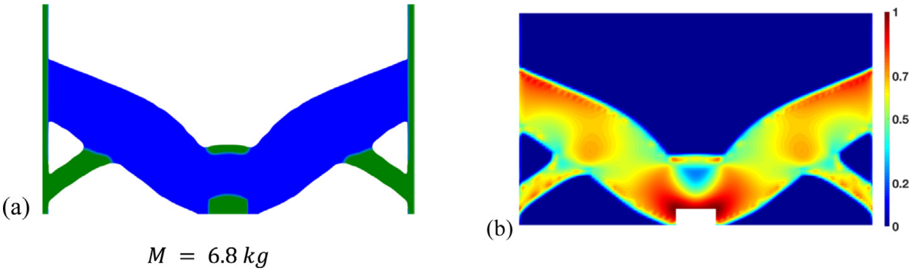

Fig. 19. Bi-clamped optimization results with failure and compliance constraints: (a) topology and material distribution; (b) normalized von Mises stress.

design due to the high thermal expansion coefficient of 304L to decrease the deformation caused by mechanical load, in the case of the Invar 36 design, the low thermal expansion only implements the tensile members.

Next, both the compliance constraint ($\bar{SE} = 139.5Nm$) and the failure constraint are considered in the optimization process, as outlined in the optimization statement (18). Figure 19(a) shows that the optimized topology and material distribution are different than in the compliance design (Fig. 17(a)). The reason for the change in the topology is that, while the 304L—with its high thermal expansion—can reduce the deformation in the compression region and, as a result, the compliance, it also increases the thermal stresses. In order to satisfy the failure constraint, this region is reduced to only two inclined members. The von Mises stress for the optimized design satisfies the constraint (Fig. 19(b)), and the optimized mass, M, is $6.8kg$.

Similar to the L-bracket case, the optimization with a single material for the bi-clamped case cannot reach the targeted compliance while satisfying the failure constraint. Thus, again, it is shown that the low compliance while satisfying the failure constraint obtained by multi-material optimization is infeasible when using a single material.

4. Conclusion

In this research, the optimized topology and composition of multi-material structures subjected to mechanical and thermal loads was studied. Interpolation schemes for the stiffness, thermal stress coefficient, allowable stress, and failure criterion were developed carefully to achieve three goals: (1) obtaining a solid-void design, (2) avoiding a material mixture away from the interfaces, and (3) satisfying the Hashin-Shtrikman bounds for the material properties at the interfaces. The interpolation schemes were incorporated in the FEM of multi-material structures, and two sets of optimization problems were developed, i.e., one with compliance minimization subjected to a mass constraint and one with mass minimization subjected to compliance and failure constraints. The effect of adding the failure constraint was studied, and it was shown that adding the failure constraint can change both the topology and the composition of the material. Next, the single-material and multi-material optimized designs were compared. Two test cases indicated that the low compliance of the multi-material designs, while satisfying the failure constraint, was infeasible using single-material domains. The findings in this research clearly demonstrate and explain the superior performance of multi-material designs for structures that are subjected to both thermal and mechanical loads and highlight the importance of simultaneous optimization of topology and material composition to fully exploit this benefit by identifying the optimized layout and location of each material.

Declaration of Competing Interest

The authors declare that they have no known competing financial interests or personal relationships that could have appeared to influence the work reported in this paper.

Acknowledgments

This work was supported by the NASA Jet Propulsion Laboratory (JPL) 2019 Summer Faculty Fellowship through the Office of the Chief Technologist, Dr. Fred Hadaegh, and the National Science Foundation (NSF) under award number 1847133 with program manager Dr. Kathryn Jablokow. The author is grateful to both JPL and the NSF for supporting this work. The author is also thankful to his JPL colleagues, Dr. Bryan McEnerney for hosting him in the Materials Engineering group at JPL, and Dr. Ryan Watkins and Dr. Adam Duran for the weekly meetings and discussions. Also, the author would like to thank Dr. Krister Svanberg for providing the MATLAB GCMMA code. The views, opinions, and/or findings expressed are those of the author and should not be interpreted as representing the official views or policies of NASA, the NSF, or the U.S. Government.

Appendix

Differentiating Eq.(8) with respect to x_{1e} yields:

$$\frac{dF^P}{dx_{1e}} = \frac{\left(F^P\right)^{1-p}}{ne}\frac{\sigma_{vm,e}}{\sigma_{ae}}\left(\frac{\sigma^r_{vm,e}}{\sigma_{ae}}\right)^{p-1}\frac{d\eta^F_e}{dx_{1e}} + \sum_{e\in Ne}\left[\frac{\left(F^P\right)^{1-p}}{ne}\frac{\eta^F_e}{\sigma_{ae}}\left(\frac{\sigma^r_{vm,e}}{\sigma_{ae}}\right)^{p-1}\frac{d\sigma_{vm,e}}{d\boldsymbol{\sigma}_{\mathbf{e}}}\bar{E}_e\bar{\mathbf{C}}\boldsymbol{B}_{\mathbf{e}}\frac{\boldsymbol{dU}_{\mathbf{e}}}{\boldsymbol{dU}}\right]\frac{d\boldsymbol{U}}{dx_{1e}} \tag{22}$$

where $\frac{d\boldsymbol{U}}{dx_{1e}}$ is obtained by differentiating Eq. (10):

$$\frac{d\boldsymbol{U}}{dx_{1e}} = \boldsymbol{K}^{-1}\left(\frac{d\boldsymbol{F}^{\boldsymbol{th}}}{dx_{1e}} - \frac{d\boldsymbol{K}}{dx_{1e}}\boldsymbol{U}\right) \tag{23}$$

Substituting Eq. (23) in Eq. (22) gives:

$$\frac{dF^P}{dx_{1e}} = \frac{\left(F^P\right)^{1-p}}{ne}\frac{\sigma_{vm,e}}{\sigma_{ae}}\left(\frac{\sigma^r_{vm,e}}{\sigma_{ae}}\right)^{p-1}\frac{d\eta^F_e}{dx_{1e}} + \sum_{e\in Ne}\left[\frac{\left(F^P\right)^{1-p}}{ne}\frac{\eta^F_e}{\sigma_{ae}}\left(\frac{\sigma^r_{vm,e}}{\sigma_{ae}}\right)^{p-1}\frac{\sigma_{vm,e}}{d\boldsymbol{\sigma}_{\mathbf{e}}}\bar{E}_e\bar{\mathbf{C}}\boldsymbol{B}_{\mathbf{e}}\frac{\boldsymbol{dU}_{\mathbf{e}}}{\boldsymbol{dU}}\right] \boldsymbol{K}^{-1}\left(\frac{d\boldsymbol{F}^{\boldsymbol{th}}}{dx_{1e}} - \frac{d\boldsymbol{K}}{dx_{1e}}\boldsymbol{U}\right) \tag{24}$$

By introducing the adjoint variable (Eq. (21)) and substituting it in Eq. (24), $\frac{dF^P}{dx_{1e}}$ in Eq. (20) is obtained.

In order to find $\frac{dF^P}{dx_{2e}}$, Eq.(8) is differentiated with respect to x_{2e}:

$$\frac{dF^P}{dx_{2e}} = \frac{\left(F^P\right)^{1-p}}{ne}\frac{\eta^F_e}{\sigma_{ae}}\left(\frac{\sigma^r_{vm,e}}{\sigma_{ae}}\right)^{p-1} \times \frac{d\sigma_{vm,e}}{d\boldsymbol{\sigma}_{\mathbf{e}}}\left(\frac{d\bar{E}_e}{dx_{2e}}\bar{\mathbf{C}}\boldsymbol{B}_{\mathbf{e}}\boldsymbol{U}_{\mathbf{e}} - \frac{d\bar{\beta}_e}{dx_{2e}}\bar{\mathbf{C}}\Phi^{\mathbf{T}}\Delta T_e\right) - \frac{\left(F^P\right)^{1-p}}{ne} \times \frac{1}{\sigma_{ae}}\left(\frac{\sigma^r_{vm,e}}{\sigma_{ae}}\right)^{p}\frac{d\sigma_{ae}}{dx_{2e}} + \sum_{e\in Ne}\left[\frac{\left(F^P\right)^{1-p}}{ne}\frac{\eta^F_e}{\sigma_{ae}}\left(\frac{\sigma^r_{vm,e}}{\sigma_{ae}}\right)^{p-1}\frac{d\sigma_{vm,e}}{d\boldsymbol{\sigma}_{\mathbf{e}}}\bar{E}_e\bar{\mathbf{C}}\boldsymbol{B}_{\mathbf{e}}\frac{\boldsymbol{dU}_{\mathbf{e}}}{\boldsymbol{dU}}\right]\frac{d\boldsymbol{U}}{dx_{2e}} \tag{25}$$

Differentiating Eq. (10) with respect to x_{2e} and substituting $\frac{d\boldsymbol{U}}{dx_{2e}}$ in Eq. (25) gives:

$$\frac{dF^P}{dx_{2e}} = \frac{\left(F^P\right)^{1-p}}{ne}\frac{\eta^F_e}{\sigma_{ae}}\left(\frac{\sigma^r_{vm,e}}{\sigma_{ae}}\right)^{p-1}\frac{d\sigma_{vm,e}}{d\boldsymbol{\sigma}_{\mathbf{e}}}\left(\frac{d\bar{E}_e}{dx_{2e}}\bar{\mathbf{C}}\boldsymbol{B}_{\mathbf{e}}\boldsymbol{U}_{\mathbf{e}} - \frac{d\bar{\beta}_e}{dx_{2e}}\bar{\mathbf{C}}\boldsymbol{\Phi}^{\mathbf{T}}\Delta T_e\right) - \frac{\left(F^P\right)^{1-p}}{ne}\frac{1}{\sigma_{ae}}\left(\frac{\sigma^r_{vm,e}}{\sigma_{ae}}\right)^{p}\frac{d\sigma_{ae}}{dx_{2e}} + \sum_{e\in Ne}\left[\frac{\left(F^P\right)^{1-p}}{ne}\frac{\eta^F_e}{\sigma_{ae}}\left(\frac{\sigma^r_{vm,e}}{\sigma_{ae}}\right)^{p-1}\frac{d\sigma_{vm,e}}{d\boldsymbol{\sigma}_{\mathbf{e}}}\bar{E}_e\bar{\mathbf{C}}\boldsymbol{B}_{\mathbf{e}}\frac{\mathbf{dU_e}}{\mathbf{dU}}\right]\boldsymbol{K}^{-1}\left(\frac{d\boldsymbol{F}^{th}}{dx_{2e}} - \frac{d\boldsymbol{K}}{dx_{2e}}\boldsymbol{U}\right) \tag{26}$$

By introducing the adjoint variable (Eq. (21)) in Eq. (26), $\frac{dF^P}{dx_{2e}}$ in Eq. (20) is obtained.

References

[1] Zegard T, Paulino GH. Bridging topology optimization and additive manufacturing. Struct Multidiscip Optim 2016;53(1):175–92. https://doi.org/10.1007/s00158-015-1274-4.

[2] Tamijani AY, Mulani SB, Kapania RK. A framework combining meshfree analysis and adaptive kriging for optimization of stiffened panels. Struct Multidiscip Optim 2014;49(4):577–94. https://doi.org/10.1007/S00158-013-0993-7.

[3] Kapania RK, Mulani SB, Tamijani A, Sunny M, Joshi P. EBF3PanelOpt: a computational design environment for panels fabricated by additive manufacturing. In: 51st AIAA Aerospace Sciences Meeting Including the New Horizons Forum and Aerospace Exposition Proceedings. p. 2013–10212.

[4] Orme M, Madera I, Gschweitl M, Ferrari M. Topology optimization for additive manufacturing as an enabler for light weight flight hardware. Designs 2018;2(4):51.

[5] Krog L, Tucker A, Kemp M, Boyd R. Topology optimization of aircraft wing box ribs. In: 10th AIAA/ISSMO multidisciplinary analysis and optimization conference. p. 1–11.

[6] Locatelli D, Mulani SB, Liu Q, Tamijani AY, Kapania RK. Supersonic Wing Optimization Using SpaRibs. NASA CR-2014-218537; 2014.

[7] Joshi P, Mulani SB, Gurav SP, Kapania RK. Design optimization for minimum sound radiation from point-excited curvilinearly stiffened panel. J Aircraft 2010;47(4):1100–10.

[8] Lazarov BS, Sigmund O, Meyer KE, Alexandersen J. Experimental validation of additively manufactured optimized shapes for passive cooling. Appl Energy 2018;226:330–9.

[9] Papapetrou VS, Patel C, Tamijani AY. Stiffness-based optimization framework for the topology and fiber paths of continuous fiber composites. Compos Part B: Eng, Accepted for Publication 2020;183:107681. https://doi.org/10.1016/j.compositesb:2019.107681.

[10] Arabnejad S, Johnston B, Tanzer M, Pasini D. Fully porous 3D printed titanium femoral stem to reduce stress-shielding following total hip arthroplasty. J Orthop Res 2017;35(8):1774–83.

[11] Bandyopadhyay A, Heer B. Additive manufacturing of multi-material structures. Mater Sci Eng: R: Rep 2018;129:1–16. https://doi.org/10.1016/j.mser.2018.04.001.

[12] Meisel N, Williams C. An investigation of key design for additive manufacturing constraints in multimaterial three-dimensional printing. J Mech Des 2015;137(11):111406. https://doi.org/10.1115/1.4030991.

[13] Zhou C, Chen Y, Yang Z, Khoshnevis B. Digital material fabrication using mask-image-projection-based stereolithography. Rapid Prototyp J 2013;19(3):153–65.

[14] Gao W, Zhang Y, Ramanujan D, Ramani K, Chen Y, Williams CB, et al. The status, challenges, and future of additive manufacturing in engineering. Comput Aided Des 2015;69:65–89.

[15] van de Werken N, Hurley J, Khanbolouki P, Sarvestani AN, Tamijani AY, Tehrani M. Design considerations and modeling of fiber reinforced 3D printed parts. Compos B Eng 2019;160:684–92. https://doi.org/10.1016/j.compositesb.2018.12.094.

[16] Hofmann DC, Roberts S, Otis R, Kolodziejska J, Dillon RP, Suh J-O, et al. Developing gradient metal alloys through radial deposition additive manufacturing. Sci Rep 2015;4(1). https://doi.org/10.1038/srep05357.

[17] Choi J-W, Kim H-C, Wicker R. Multi-material stereolithography. J Mater Process Technol 2011;211(3):318–28. https://doi.org/10.1016/j.jmatprotec.2010.10.003.

[18] Hofmann DC, Kolodziejska J, Roberts S, Otis R, Dillon RP, Suh J-O, et al. Compositionally graded metals: a new frontier of additive manufacturing. J Mater Res 2014;29(17):1899–910.

[19] Bruet BJF, Song J, Boyce MC, Ortiz C. Materials design principles of ancient fish armour. Nat Mater 2008;7(9):748–56. https://doi.org/10.1038/nmat2231.

[20] Tammas-Williams S, Todd I. Design for additive manufacturing with site-specific properties in metals and alloys. Scr Mater 2017;135:105–10. https://doi.org/10.1016/j.scriptamat.2016.10.030.

[21] Loh GH, Pei E, Harrison D, Monzón MD. An overview of functionally graded additive manufacturing. Addit Manuf 2018;23:34–44. https://doi.org/10.1016/j.addma.2018.06.023.

[22] Suresh S, Giannakopoulos AE, Alcalá J. Spherical indentation of compositionally graded materials: theory and experiments. Acta Mater 1997;45(4):1307–21. https://doi.org/10.1016/s1359-6454(96)00291-1.

[23] Giannakopoulos AE, Suresh S, Finot M, Olsson M. Elastoplastic analysis of thermal cycling: layered materials with compositional gradients. Acta Metall Mater 1995;43(4):1335–54. https://doi.org/10.1016/0956-7151(94)00360-t.

[24] Thomsen J. Topology optimization of structures composed of one or two materials. Struct Optim 1992;5(1):108–15. https://doi.org/10.1007/bf01744703.

[25] Sigmund O. Design of multiphysics actuators using topology optimization – Part II: two-material structures. Comput Methods Appl Mech Eng 2001;190(49–50):6605–27. https://doi.org/10.1016/s0045-7825(01)00252-3.

[26] Sigmund O, Torquato S. Design of materials with extreme thermal expansion using a three-phase topology optimization method. J Mech Phys Solids 1997;45(6):1037–67. https://doi.org/10.1016/S0022-5096(96)00114-7.

[27] Sigmund O, Maute K. Topology optimization approaches A comparative review. Struct Multidiscip Optim 2013;48(6):1031–55. https://doi.org/10.1007/s00158-013-0978-6.

[28] Hashin Z, Shtrikman S. A variational approach to the theory of the elastic behaviour of multiphase materials. J Mech Phys Solids 1963;11(2):127–40.

[29] Bendsøe MP, Sigmund O. Material interpolation schemes in topology optimization. Arch Appl Mech 1999;69(9-10):635–54.

[30] Yin L, Ananthasuresh GK. Topology optimization of compliant mechanisms with multiple materials using a peak function material interpolation scheme. Struct Multidiscip Optim 2001;23(1):49–62. https://doi.org/10.1007/s00158-001-0165-z.

[31] Park J, Sutradhar A. A multi-resolution method for 3D multi-material topology optimization. Comput Methods Appl Mech Eng 2015;285:571–86. https://doi.org/10.1016/j.cma.2014.10.011.

[32] Taheri AH, Suresh K. An isogeometric approach to topology optimization of multi-material and functionally graded structures. Int J Numer Meth Eng 2017;109(5):668–96. https://doi.org/10.1002/nme.v109.510.1002/nme.5303.

[33] Zhou S, Wang MY. Multimaterial structural topology optimization with a generalized Cahn-Hilliard model of multiphase transition. Struct Multidiscip Optim 2006;33(2):89–111. https://doi.org/10.1007/s00158-006-0035-9.

[34] Wang MY, Zhou S. Synthesis of shape and topology of multi-material structures with a phase-field method. 2004;11(2-3):117–38. doi: 10.1007/s10820-005-3169-y.

[35] Huang X, Xie YM. Bi-directional evolutionary topology optimization of continuum structures with one or multiple materials. Comput Mech 2009;43(3):393–401. https://doi.org/10.1007/s00466-008-0312-0.

[36] Radman A, Huang X, Xie YM. Topological design of microstructures of multi-phase materials for maximum stiffness or thermal conductivity. 2014;91:266–73. doi: 10.1016/j.commatsci.2014.04.064.

[37] Maleki Jebeli S, Shariat Panahi M. An evolutionary approach for simultaneous optimization of material property distribution and topology of FG structures. 2015;32(2):234–57. doi: 10.1108/ec-07-2013-0188.

[38] Wang MY, Wang X. "Color" level sets: a multi-phase method for structural topology optimization with multiple materials. Comput Methods Appl Mech Eng 2004;193(6):469–96. https://doi.org/10.1016/j.cma.2003.10.008.

[39] Wei P, Wang MY. Piecewise constant level set method for structural topology optimization. 2009;78(4):379–402. doi: 10.1002/nme.2478.

[40] Wang MY, Chen S, Wang X, Mei Y. Design of multimaterial compliant mechanisms using level-set methods. J Mech Des 2005;127(5):941–56. https://doi.org/10.1115/1.1909206.

[41] Luo Z, Tong L, Luo J, Wei P, Wang MY. Design of piezoelectric actuators using a multiphase level set method of piecewise constants. 2009;228(7):2643–59. doi: 10.1016/j.jcp.2008.12.019.

[42] Zhuang C, Xiong Z, Ding H. Topology optimization of multi-material for the heat conduction problem based on the level set method. 2010;42(9):811–31. doi: 10.1080/03052150903443780.

[43] Vermaak N, Michailidis G, Parry G, Estevez R, Allaire G, a Bréchet Y. Material interface effects on the topology optimizationof multi-phase structures using a level set method. 2014;50(4):623–44. doi: 10.1007/s00158-014-1074-2.

[44] Liu P, Luo Y, Kang Z. Multi-material topology optimization considering interface behavior via XFEM and level set method. Comput Methods Appl Mech Eng 2016;308:113–33. https://doi.org/10.1016/j.cma.2016.05.016.

[45] Wang Y, Luo Z, Kang Z, Zhang N. A multi-material level set-based topology and shape optimization method. Comput Methods Appl Mech Eng 2015;283:1570–86. https://doi.org/10.1016/j.cma.2014.11.002.

[46] Duysinx P, Bendsøe MP. Topology optimization of continuum structures with local stress constraints. Int J Numer Meth Eng 1998;43(8):1453–78.

[47] Bruggi M. On an alternative approach to stress constraints relaxation in topology optimization. Struct Multidiscip Optim 2008;36(2):125–41.

[48] Le C, Norato J, Bruns T, Ha C, Tortorelli D. Stress-based topology optimization for continua. Struct Multidiscip Optim 2010;41(4):605–20.

[49] Yang RJ, Chen CJ. Stress-based topology optimization. Struct Optim 1996;12(2-3):98–105.

[50] Duysinx P, Sigmund O. New developments in handling stress constraints in optimal material distribution. In: 7th AIAA/USAF/NASA/ISSMO symposium on multidisciplinary analysis and optimization. p. 4906.

[51] Holmberg E, Torstenfelt B, Klarbring A. Stress constrained topology optimization. Struct Multidiscip Optim 2013;48(1):33–47. https://doi.org/10.1007/s00158-012-0880-7.

[52] Pereira JT, Fancello EA, Barcellos CS. Topology optimization of continuum structures with material failure constraints. Struct Multidiscip Optim 2004;26(1):50–66. https://doi.org/10.1007/s00158-003-0301-z.

[53] da Silva GA, Aage N, Beck AT, Sigmund O. Three-dimensional manufacturing tolerant topology optimization with hundreds of millions of local stress constraints. Int J Numer Meth Eng 2021;122(2):548–78. https://doi.org/10.1002/nme.v122.210.1002/nme.6548.

[54] Senhora FV, Giraldo-Londoño O, Menezes IFM, Paulino GH. Topology optimization with local stress constraints: a stress aggregation-free approach. Struct Multidiscip Optim 2020;62(4):1639–68. https://doi.org/10.1007/s00158-020-02573-9.

[55] Emmendoerfer H, Fancello EA. A level set approach for topology optimization with local stress constraints. Int J Numer Meth Eng 2014;99(2):129–56. https://doi.org/10.1002/nme.4676.

[56] Ramani A. Multi-material topology optimization with strength constraints. Struct Multidiscip Optim 2011;43(5):597–615.

[57] Guo X, Zhang W, Zhong W. Stress-related topology optimization of continuum structures involving multi-phase materials. 2014;268:632–55. doi: 10.1016/j.cma.2013.10.003.

[58] Conlan-Smith C, James KA. A stress-based topology optimization method for heterogeneous structures. Struct Multidiscip Optim 2019;60(1):167–83. https://doi.org/10.1007/s00158-019-02207-9.

[59] Faure A, Michailidis G, Parry G, Vermaak N, Estevez R. Design of thermoelastic multi-material structures with graded interfaces using topology optimization. Struct Multidiscip Optim 2017;56(4):823–37. https://doi.org/10.1007/s00158-017-1688-2.

[60] Deaton JD, Grandhi RV. Stress-based design of thermal structures via topology optimization. Struct Multidiscip Optim 2016;53(2):253–70.

[61] Gao T, Zhang W. Topology optimization involving thermo-elastic stress loads. Struct Multidiscip Optim 2010;42(5):725–38. https://doi.org/10.1007/s00158-010-0527-5.

[62] Gao T, Xu P, Zhang W. Topology optimization of thermo-elastic structures with multiple materials under mass constraint. 2016;173:150–60. doi: 10.1016/j.compstruc.2016.06.002.

[63] Wu C, Fang J, Li Q. Multi-material topology optimization for thermal buckling criteria. Comput Methods Appl Mech Eng 2019;346:1136–55. https://doi.org/10.1016/j.cma.2018.08.015.

[64] Xu Z, Zhang W, Gao T, Zhu J. A B-spline multi-parameterization method for multi-material topology optimization of thermoelastic structures. Struct Multidiscip Optim 2020;61(3):923–42. https://doi.org/10.1007/s00158-019-02464-8.

[65] Giraldo-Londoño O, Mirabella L, Dalloro L, Paulino GH. Multi-material thermomechanical topology optimization with applications to additive manufacturing: design of main composite part and its support structure. Comput Methods Appl Mech Eng 2020;363:112812. https://doi.org/10.1016/j.cma.2019.112812.

[66] Stolpe M, Svanberg K. An alternative interpolation scheme for minimum compliance topology optimization. Struct Multidiscip Optim 2001;22(2):116–24. https://doi.org/10.1007/s001580100129.

[67] Bruyneel M, Duysinx P. Note on topology optimization of continuum structures including self-weight. Struct Multidiscip Optim 2005;29(4):245–56. https://doi.org/10.1007/s00158-004-0484-y.

[68] Dieter GE, Bacon D. Mechanical metallurgy. New York: McGraw-hill; 1986.

[69] Bruns TE, Tortorelli DA. Topology optimization of non-linear elastic structures and compliant mechanisms. Comput Methods Appl Mech Eng 2001;190(26–27):3443–59. https://doi.org/10.1016/s0045-7825(00)00278-4.

[70] Svanberg K. A class of globally convergent optimization methods based on conservative convex separable approximations. SIAM J Optim 2002;12(2):555–73.

[71] Lee E, James KA, Martins JRRA. Stress-constrained topology optimization with design-dependent loading. Struct Multidiscip Optim 2012;46(5):647–61. https://doi.org/10.1007/s00158-012-0780-x.

[72] Wang Z, Palmer TA, Beese AM. Effect of processing parameters on microstructure and tensile properties of austenitic stainless steel 304L made by directed energy deposition additive manufacturing. Acta Mater 2016;110:226–35. https://doi.org/10.1016/j.actamat.2016.03.019.

[73] Vinogradov A, Hashimoto S, Kopylov VI. Enhanced strength and fatigue life of ultra-fine grain Fe–36Ni Invar alloy. 355(1–2) 2003;355(1-2):277–85. https://doi.org/10.1016/S0921-5093(03)00082-0.

[74] Bendsoe MP, Sigmund O. Topology optimization: theory, methods, and applications. Springer Science & Business Media; 2013.